



This open access document is published as a preprint in the Beilstein Archives with doi: 10.3762/bxiv.2019.42.v1 and is considered to be an early communication for feedback before peer review. Before citing this document, please check if a final, peer-reviewed version has been published in the Beilstein Journal of Nanotechnology.

This document is not formatted, has not undergone copyediting or typesetting, and may contain errors, unsubstantiated scientific claims or preliminary data.

Preprint Title Design and facile synthesis of defect rich C-MoS₂/rGO nanosheets for enhanced lithium-sulfur battery performance

Authors Chengxiang Tian, Juwei Wu, Zheng Ma, Bo Li, Pengcheng Li, Xiaotao Zu and xia xiang

Article Type Full Research Paper

Supporting Information File 1 Supplementary material.docx; 1.9 MB

ORCID® iDs xia xiang - <https://orcid.org/0000-0002-4042-1016>

Design and facile synthesis of defect rich C-MoS₂/rGO nanosheets for enhanced lithium-sulfur battery performance

Chengxiang Tian^a, Juwei Wu^a, Zheng Ma^a, Bo Li^a, Pengcheng Li^a, Xiaotao Zu^a,

Xia Xiang^{a1}

^a School of Physics, University of Electronic Science and Technology of China, Chengdu 610054, China

Abstract

Reliable design and fabrication of advanced electrode materials are vital for developing lithium sulfur batteries. In this contribution, we report a simple one-step hydrothermal strategy for fabrication of a C-MoS₂/rGO composite with both large surface area and high porosity. Double modified defect-rich MoS₂ nanosheets are successfully prepared by introducing graphene oxide (GO) and amorphous carbon. The conductivity and structural stabilization of the cathodes can be improved owing to combination between the amorphous carbon and rGO, which could also restrain the dissolution of polysulfides. After annealing at different temperatures, it is found that the C-MoS₂/rGO-6-S composite annealed at 600 °C delivers noticeably enhanced the performance of lithium-sulfur batteries, with a high specific capacity of 572 mAh·g⁻¹ at 0.2C after 550 cycles, and 551 mAh·g⁻¹ even at 2C, much better than those of MoS₂-S nanosheets (249 mAh·g⁻¹ and 149 mAh·g⁻¹) and C-MoS₂/rGO-S composite (334 mAh·g⁻¹ and 382 mAh·g⁻¹). Our intended electrode design protocol and annealing

¹ Corresponding authors: xiaxiang@uestc.edu.cn (Xia Xiang), Tel:86-28-8320-2130

process may pave the way for the construction of other high-performance metal disulphide electrode for electrochemical energy storage.

Keywords

MoS₂, Double modification, Annealing, Lithium sulfur battery

Introduction

Lithium-sulfur (Li-S) batteries have attracted great attentions because of its high energy density (2600 W h kg⁻¹) and specific capacity (1675 mA h g⁻¹), low cost, and abundant reserves of elemental sulfur[1, 2]. Nevertheless, the development of Li-S batteries encounters various technical challenges. The intrinsic insulation properties of discharge products (Li₂S₂ and Li₂S) and sulfur result in a slow charge and discharge process and a low specific capacity[3]. The production of intermediate products (Li₂S_n, where 3 ≤ n ≤ 8) during battery charge and discharge are electrolyte soluble and can also migrate to the lithium metal anode and precipitate there [4, 5]. The decay of electrochemically active lithium polysulfides causes a rapid capacity degradation during charge and discharge process.

In order to overcome the problems above, great efforts have been applied to enhance the performance of Li-S batteries, including combining conductive materials with sulfur [6-8], constructing Li₂S_n blocking interlayers[9-11], and applying functional separators[12-15]. Although there are many methods, the most usual strategy is to combine sulfur with various carbon materials owing to their excellent conductivity and flexible nanostructures. However, the capacity of carbon and sulfur composite cathodes generally fades rapidly during long-term cycling, because the carbon materials can provide inferior physical adsorption to the polar Li₂S_n[16]. Once Li₂S_n is solvated, it dissolves easily in the electrolyte from the electrode surface and continues to disperse. Consequent reutilization of Li₂S_n will become very hard due to the repulsion between the nonpolar conductive surface and the polar reactants [17].

Two-dimensional layered transition metal dichalcogenides (TMDs), as a strong candidate in the search for energy storage and catalysts, can provide good performance

at low cost[18-20]. In particular, MoS₂ has attracted the most attention owing to the high electrochemical activity associated with the sulfur deficiencies[5]. It has been reported that MoS₂ nanosheets reveal individual performance in the oil hydrodesulphurization process to catalyze sulfur species[21, 22], indicating their wide application for Li–S batteries. Therefore, double modification of defect-rich MoS₂ nanosheets with carbon materials should be a very hopeful strategy to increase the performance of sulfur cathodes.

In this work, we firstly present a double carbon network modification method for defect-rich MoS₂ anodes by introducing amorphous carbon and rGO via a one-step hydrothermal method. We concentrate on not only the material design based on both structure and chemical composition but also the development of MoS₂ electrocatalysts. Firstly, the MoS₂ nanosheets are interconnected with rGO and then well covered by the carbon layer. This means that overall connected conductive networks are well formed by the combination of amorphous carbon layer and rGO. Secondly, the existence of a great number of defects in the ultrathin MoS₂ nanosheets leads to partial breaking of the catalytically inert basal planes, owing to exposure of extra active edge sites. Thirdly, annealing of C-MoS₂/rGO composite at different temperatures has also been investigated. The annealed composites can improve crystallinity and increases the bonding energy, and also improve the stability with the high specific capacity. The defect-rich C-MoS₂/rGO prepared in this work can not only kinetically accelerate the sulfur redox reactions but also chemically adsorb LiPSs. In addition, rGO and carbon layer can also enhance the conductivity of the C-MoS₂/rGO. Therefore, the C-MoS₂/rGO, as an efficient sulfur host, could exhibit excellent electrochemical performance.

2 Experiment section

2.1 Preparation of defect-rich C-MoS₂/rGO nanosheets

For the synthesis of the C-MoS₂/rGO nanosheets, 1.23 g hexaammonium heptamolybdate tetrahydrate, 0.89 g of glucose, and 2.28 g thiourea were dissolved in 25 mL of deionized water to form Solution A; 0.03 g of GO was dissolved into 10 mL of deionized water by ultrasonic to form the Solution B. Then solution A is mixed with solution B and stirred for 30 min. Subsequently, the mixture was transferred to a 50 mL Teflon-lined stainless steel autoclave and retained at 200 °C for 24 h. After cooling naturally, the product was washed with deionized water and absolute ethanol for several times and dried at 60 °C in vacuum. For comparison, the pristine MoS₂ were synthesized using an identical process without GO or glucose. Then the obtained composites were annealed at 400, 600 and 800 °C for 6 hours in 10% H₂/Ar atmosphere to improve the crystallinity. After thermal annealing, the samples were labeled as C-MoS₂/rGO-4, C-MoS₂/rGO-6, and C-MoS₂/rGO-8, respectively.

2.2 Preparation of sulfur composite

MoS₂-S, C-MoS₂/rGO-S, C-MoS₂/rGO-4-S, C-MoS₂/rGO-6-S, C-MoS₂/rGO-8-S composites were fabricated by the melt-diffusion method. The mixture of sulfur and pristine MoS₂, C-MoS₂/rGO and annealed composites (C-MoS₂/rGO-4, C-MoS₂/rGO-6, C-MoS₂/rGO-8) with a 3 : 1 mass ratio was calcined at 155 °C for 12 h in a sealed vessel.

2.3 Materials characterization

The structure and morphology were investigated by field emission scanning electron microscopy (FE-SEM) (INSPECT F50) and transmission electron microscopy (TEM) (TEM, ZISSLibra 200). A powder X-ray diffraction (XRD) was conducted to determine the phase of the as-synthesized composites, with Cu K α radiation operated at 40 kV and 30 mA. X-ray photoelectron spectroscopy (XPS) analysis were performed on Kratos AXIS Ultra DLD instrument using monochromated Al K α X-rays as the excitation source. Raman spectra were collected using a Witec alpha 300M+ instrument with an excitation laser wavelength of 488 nm. Nitrogen adsorption–desorption isotherm measurements were conducted at 77 K using a micromeritics system (JW-BK132F). The contents of amorphous carbon, rGO and sulfur in the samples were analyzed by thermogravimetric (TGA) on a Netzsch STA 449C analyzer in air for the amorphous carbon and rGO or in N₂ atmosphere for the sulfur at a temperature ramp rate of 10 °C min⁻¹.

2.4 Lithium polysulfide adsorption tests

The concentration of the fabricated Li₂S₆ solution was 3 mM by dissolving stoichiometric amounts of lithium sulfide (Li₂S) and sulfur with a molar ratio of 1 : 5 in 1,3-dioxolane (DOL) and dimethoxymethane (DME) (1 : 1 by volume) and then stirring for overnight in a glovebox. After that, 5 mg of pristine MoS₂, C-MoS₂/rGO and annealed composites were added to the Li₂S₆ solution (3 mL) as the adsorbents, respectively.

2.5 Cell assembly and electrochemical measurements

The working electrodes were prepared by casting the slurry of 80 wt% active materials (MoS₂-S, C-MoS₂/rGO-S, C-MoS₂/rGO-4-S, C-MoS₂/rGO-6-S, C-MoS₂/rGO-8-S), 10 wt% Super P and 10 wt% polyvinylidene fluoride (PVDF) in N-methyl-2-pyrrolidone (NMP) on an Al foil current collector. Subsequently, the electrodes were dried in vacuum at 60 °C for 12 h.

The electrode was manufactured in a coin-type cell (CR 2032) in an argon-filled glove box (O₂ < 0.1 ppm, H₂O < 0.1 ppm). The electrolyte was 1 M bis(trifluoromethane) sulfonamide lithium salt (LITFSI) dissolved in a mixed solution of dimethyl ether (DME) and 1,3-dioxolane (DOL) (1:1, v/v) with 2 wt% LiNO₃. The recharge properties and cyclic voltammetry tests were carried out on a LAND battery cycler (CT2001A) corresponding voltage range of 1.7 to 2.9 V (vs. Li/Li⁺). The specific capacity was calculated based on mass of the sulfur. Cyclic voltammetry (CV) tests were carried out between 1.6 and 2.9 V at a scan rate of 0.1 mV s⁻¹. The electrochemical impedance spectroscopy (EIS) measurements were achieved at the open circuit potential between 0.01 Hz and 100 kHz. All the tests were completed at room temperature.

3 Results and discussion

The preparation schematic of the C-MoS₂/rGO composite is shown in Fig. 1. The C-MoS₂/rGO composite is synthesized by the simple and efficient hydrothermal followed by annealing process.

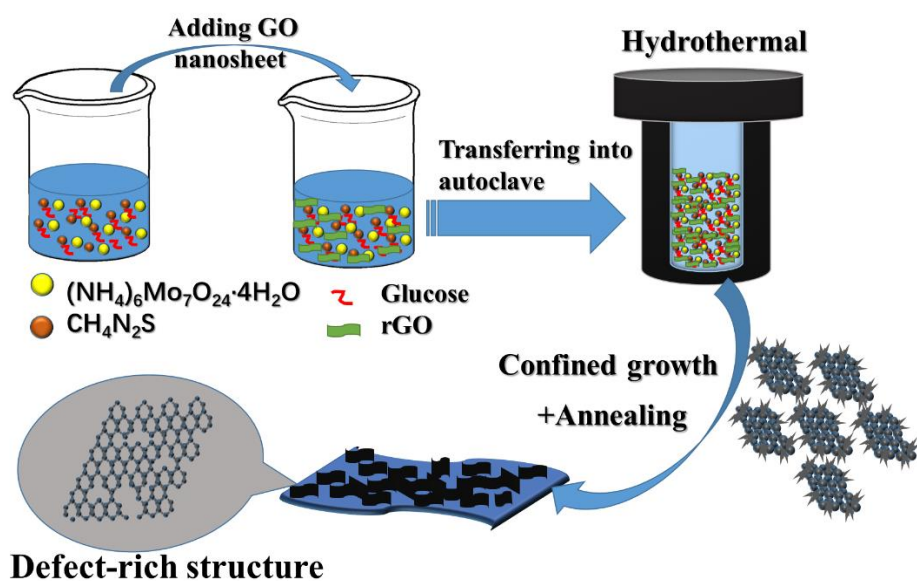


Fig. 1 Schematic illustration of synthesis of C-MoS₂/rGO composite.

The SEM image in Fig. 2a clearly reveals the morphology of the pristine ultrathin MoS₂ nanosheets. The apparent corrugations and ripples can be shown and the lateral size of the nanosheets is 200–300 nm. A corresponding TEM image also verifies the ultrathin nanosheets morphology as shown in Fig. 2b. Due to the addition of amorphous carbon and rGO, the size of C-MoS₂/rGO nanosheets is obviously smaller as shown in Fig. 2c-d. However, the morphology of nanosheets doesn't change even after annealing at 800 °C as shown in Fig. S1a-d.

Additionally, interplanar spacing of 0.27 nm can be observed in Fig. 2e and 2g. Numerous distortions and dislocations can be observed, which indicates a defect-rich structure as shown in the white circle in Fig. 2e and 2g. The similar phenomenon is also observed for the C-MoS₂/rGO-4 and C-MoS₂/rGO-8 as shown in Fig. S1e and S1g. The additional edges are generated by breaking of the basal planes due to disordered atomic arrangement, which is beneficial for catalyst the polysulfide. Furthermore, the typical lamellar structure with interlayer spacing of 0.65 nm and 0.66 nm can be observed in

Fig. 2f and 2h; the layer-to-layer spacing is slightly larger than the spacing of 6.2 nm in bulk MoS₂ [23-25]. The crystal nanosheets along the edge are irregular, which can also be ascribed to the successful introduction of rich defects, as indicated by the arrows in the images. Therefore, better energy storage property may be anticipated from double modification of defect-rich MoS₂ nanosheets.

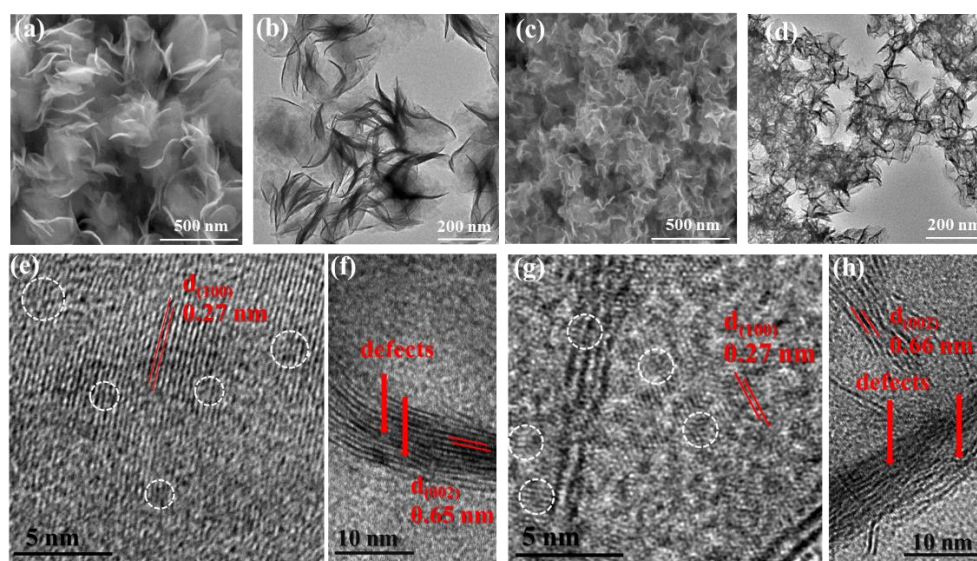


Fig. 2 Morphological images of the pristine MoS₂ (a) SEM image, (b) TEM image, and (e-f) HRTEM images; Morphological images of the C-MoS₂/rGO composite (c) SEM image, (d) TEM image, (g-h) HRTEM images.

After annealing, the lattice fringes distance is further increased to about 0.68 nm, and the fringes of the edges are also apparently curled as shown in Fig. 3a-d. The lattice fringes distance doesn't change even after annealing at 800 °C, as shown in Fig. S1f and S1h. The EDS spectrum demonstrates the existence of the elements S, Mo, and C in Fig. 3e. A typical TG analysis (Fig. 3f) is performed in air from room temperature to 800 °C. The MoS₂ and carbon are oxidized to MoO₃ and CO₂ in this temperature range [3, 26]. After calculation, the mass percentages of MoS₂ in the C-MoS₂/rGO and C-

MoS₂/rGO-6 composite are about 80 wt.% and 78 wt.%, respectively. The content decrease of C-MoS₂/rGO-6 composite may be due to the MoS₂ decomposes in 10% H₂/Ar atmosphere during annealing treatment when the temperature is higher than 600 °C[27, 28]. Meanwhile, the homogeneous diffusion of the elements are confirmed by the selected element mappings as shown in Fig. 3g-j.

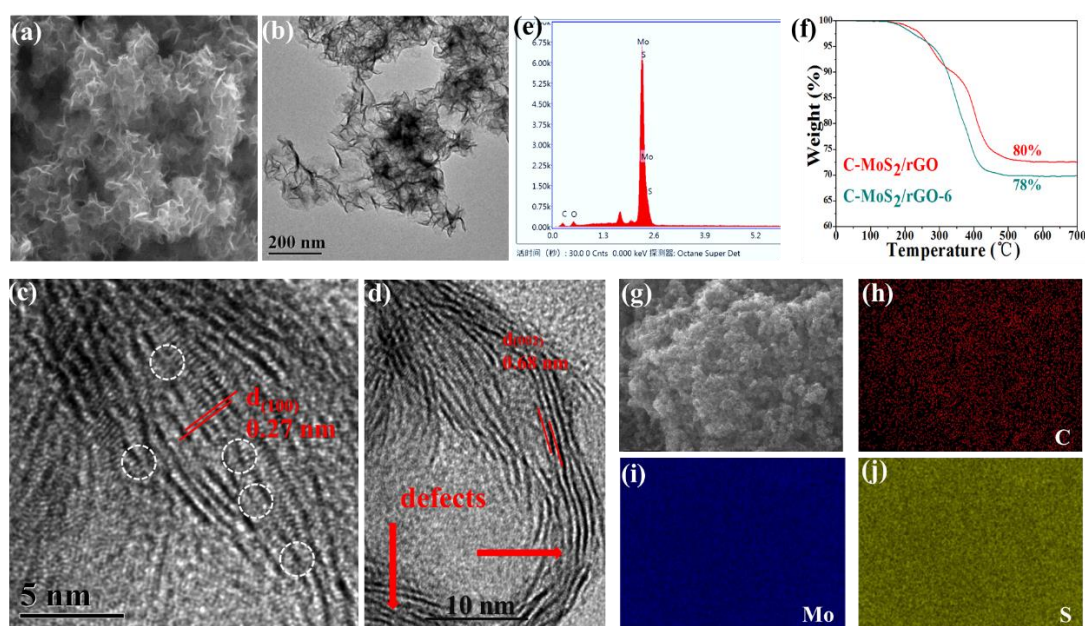


Fig. 3 Morphological images of the annealed C-MoS₂/rGO-6 composite: (a) SEM; (b)TEM; (c-d) HRTEM; (e) EDS spectrum, (f) TG analysis curve, (g-j) Element mapping images of Mo, S, and C.

Fig. 4a shows the XRD patterns of the pristine MoS₂, C-MoS₂/rGO and annealed C-MoS₂/rGO-6 composites. For the pristine MoS₂, the diffraction peaks can be well indexed to the 2H-MoS₂ phase (JCPDS 73-1508). Meanwhile, the defect-rich structure causes the formation of smaller nanosheets along the basal planes in Fig. 2e, which is coherent with the remarkable broadening of (110) and (100) diffraction peaks. The peak at about 14.39°, which corresponds to the (002) planes, is shown in the XRD pattern of

the pristine MoS₂ but not in that of the C-MoS₂/rGO and C-MoS₂/rGO-6 composite. This is ascribed carbon layer and rGO nanosheets which can reduce the stacking of MoS₂ layers, causing the invisible of these characteristic peaks. A analogous phenomenon has been described in other works [29, 30]. The broad and weak peak at 17.65° for C-MoS₂/rGO composite might be contributed to the spacing between the MoS₂ nanosheet and carbon layer[31, 32] and it disappeared after annealing. Compared with C-MoS₂/rGO, it is noticeable that the diffraction peaks of the C-MoS₂/rGO-6 become sharper, which also indicates that the annealing treatment improves the crystallinity of the composite.

Fig. 4b and Fig. S2 show the Raman spectra of the pristine MoS₂, C-MoS₂/rGO, C-MoS₂/rGO-6, C-MoS₂/rGO-4 and C-MoS₂/rGO-8 composites. Two clear peaks at about 378 cm⁻¹ and 404 cm⁻¹ are showed in all curves of MoS₂, consistent with the in-plane E_{2g}^1 and out-of-plane A_{1g} of the pristine MoS₂, respectively[33]. In addition to these peaks from pristine MoS₂, the Raman spectra of C-MoS₂/rGO, C-MoS₂/rGO-6, C-MoS₂/rGO-4 and C-MoS₂/rGO-8 exhibit two broad bands at 1363 cm⁻¹ (D-band) and 1587 cm⁻¹ (G band) resulted from in-plane vibrations and defect-induced vibrations of sp² hybridized carbon in amorphous carbon and rGO [26].

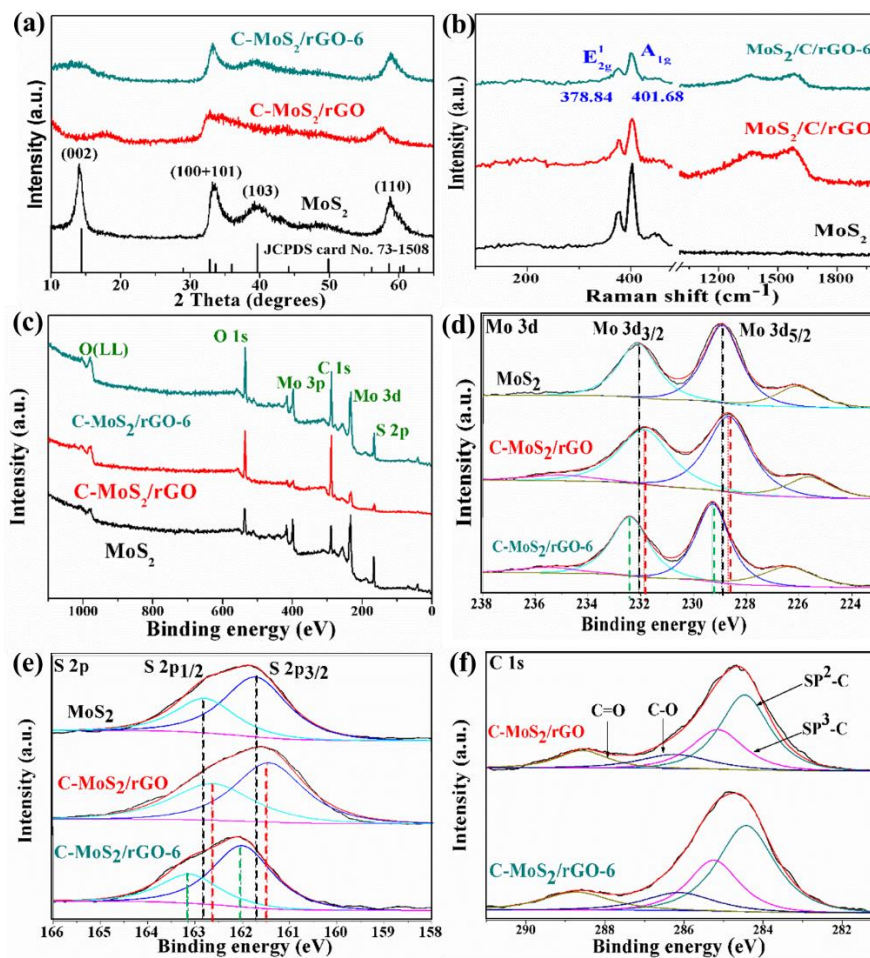


Fig. 4 (a) XRD patterns, (b) Raman spectra, (c) Full scan XPS spectra and high resolution XPS spectra of (d) Mo 3d and (e) S 3d of pristine MoS₂, C-MoS₂/rGO and C-MoS₂/rGO-6 composites, and (f) high resolution XPS spectra of C 1s C-MoS₂/rGO and C-MoS₂/rGO-6 composites, respectively.

The surface composition of composites is analyzed by XPS. The survey spectrum confirms that the expected elements in composite are C, Mo, O, and S (Fig. 4c), which is consistent with the above EDS analysis. The two peaks of the pristine MoS₂ at 228.9 and 232.1 eV in Fig. 4d are assigned to Mo 3d_{5/2} and 3d_{3/2} binding energies for Mo⁴⁺ oxidation state, respectively[20]. The two peaks at 162.78 and 161.7 eV are attributed to the S 2p_{1/2} and S 2p_{3/2} orbital of divalent sulfide ions (S²⁻) of MoS₂, as shown in

Fig.4e [34]. However, the binding energies of Mo $3d_{5/2}$ and Mo $3d_{3/2}$ in C-MoS₂/rGO composite shift to 228.6 and 231.8 eV, respectively (Fig 4d). Similarly, the binding energies of S $2p_{3/2}$ and S $2p_{1/2}$ in the C-MoS₂/rGO composite is reduced by about 0.2 eV relative to that in the pristine MoS₂. This can be attributed to the interactions of MoS₂, amorphous carbon and rGO, which weakens the binding energy of Mo and S[35]. However, after the annealing process, the binding energies of Mo $3d_{5/2}$, Mo $3d_{3/2}$, S $2p_{3/2}$ and S $2p_{1/2}$ in the C-MoS₂/rGO-6 composite increased by about 0.4 and 0.3 eV relative to that in the pristine MoS₂. The increased binding energy of the C-MoS₂/rGO-6 may be owing to the improved crystallinity after annealing, which is consistent with the results of XRD. These results strongly suggest the existence of electronic interactions between amorphous carbon and MoS₂, which implies the establishment of coupling interfaces[36]. This interaction not only improves the rate of catalytic polysulfide conversion but also effectively utilizes the conductivity of carbon, which is the goal of designing materials that overcome the inherent defects of lithium-sulfur batteries. This is consistent with the experimental results.

The detected peak of high resolution C 1s spectrum can be deconvoluted into four peaks, as shown in Fig. 4f. The peak at 284.5 eV with high intensity indicates that most C atoms in composites can be assigned to a conjugated honeycomb lattice and connected to graphite like sp² carbon[29]. The peaks located at 285.1 and 286.2 eV corresponds to the binding energy of carbon in C–C bonds and C–O bonds, respectively, owing to an amorphous carbon layer originated from glucose. The two weak peaks originated from the C–O and C=O bonds illustrate that the oxygen-containing

functional groups are almost removed during the hydrothermal synthesis and annealing process[37].

Full nitrogen sorption isotherms of the composites were tested to obtain the specific surface area and the pore size distribution. A type-IV isotherm with a type-H3 hysteresis loop in the relative pressure range of 0.45–1.0 P/P_0 suggests the presence of mesoporous structure, as shown in Fig. 5a.

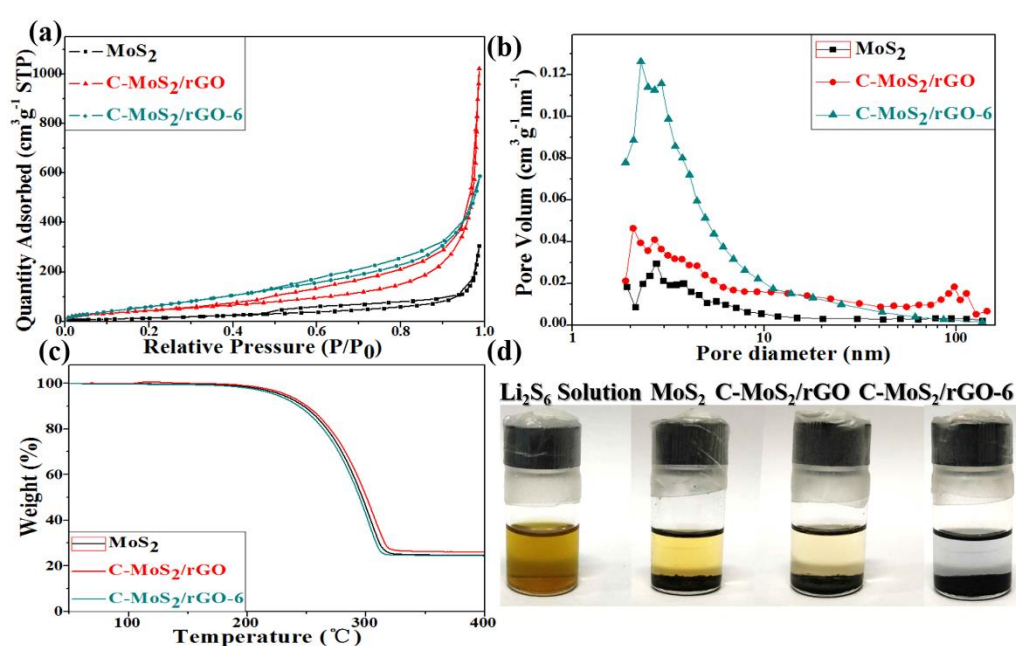


Fig. 5 (a) N₂ adsorption/desorption isotherms and (b) corresponding pore size distributions of the pristine MoS₂, C-MoS₂/rGO and C-MoS₂/rGO-6 composites. (c) TG curves of MoS₂-S, C-MoS₂/rGO-S and C-MoS₂/rGO-6-S composites; (d) Photos of the Li₂S₆ solution after 12 h adsorption experiments with same amount of pristine MoS₂, C-MoS₂/rGO and C-MoS₂/rGO-6 composites.

Consequently, the specific surface area is calculated to be 131.72, 300.64, 539.16 m² g⁻¹ by using the Brunauer-Emmett Teller (BET) method. The pore size distribution obtained from the Barrett-Joyner-Halenda (BJH) method is given in Fig. 5b. This

difference can be ascribed to the nanostructure of smaller MoS₂ nanosheet and the assistance of amorphous carbon and rGO. The obtained high specific surface area of C-MoS₂/rGO-6 composite is mainly attributed to the following two aspects: a large amount of amorphous carbon is reduced by hydrogen to cause further increase of carbon defects; and the crystallinity of the MoS₂ nanosheets is further improved. This is consistent with the results of XRD and Raman. The pore-size distribution curve of composites analyzed through BJH method exhibits a sharp peak at 3 nm and another broad peak at 40 nm compared with pristine MoS₂ and C-MoS₂/rGO, further demonstrating the mesoporous structure C-MoS₂/rGO-6. The specific surface area (130.57 m² g⁻¹) of C-MoS₂/rGO-6-S composite is significantly smaller compared to the C-MoS₂/rGO-6 as shown in Fig. S3a. Additionally, the broad pore size distribution, ranging from 2 to 10 nm, diminished obviously in the C-MoS₂/rGO-6-S composite (Fig. S3b) compared to the C-MoS₂/rGO-6 composite, which indicates that the sulfur element can be successfully dispersed into the mesoporous of the C-MoS₂/rGO-6 composite.

The sulfur contents in the different composites as tested by TGA were about 75 wt% as shown in Fig. 5c. Polysulfides adsorption capability of the pristine MoS₂, C-MoS₂/rGO and C-MoS₂/rGO-6 is also examined as shown in Fig. 5d and Fig. S4a. After immersion in the 3 mL Li₂S₆ solution (3 mmol L⁻¹ in 1:1 (v/v) DME/DOL) for 12 h, C-MoS₂/rGO-6 renders the Li₂S₆ solution almost completely colorless while the pristine MoS₂ remains a stronger yellow-gold than C-MoS₂/rGO composite, which could be attributed to the porous structure and high specific surface area of the C-MoS₂/rGO-6

composite. Additionally, the Li_2S_6 in the solution is still not completely absorbed by the C-MoS₂/rGO-4 and C-MoS₂/rGO-8 composites. Consequently, the C-MoS₂/rGO-6 decolorized solution suggests the superior polysulfide adsorption capability of the C-MoS₂/rGO-6 composite than that of the MoS₂ and other composites.

In order to illustrate the better electrochemical performance of the composites, the three samples of MoS₂-S, C-MoS₂/rGO-S, C-MoS₂/rGO-6-S were used as cathodes and evaluated using CR2032 coin cells. The obvious redox peaks show the multiple reaction mechanism of sulfur cathodes in Li-S batteries, as shown in Fig. 6a. Two explicit reduction peaks located at 2.25 V and 2.02 V corresponds to the cathodic scanning. The peak at 2.25 V is relate to the reduction of cyclic S₈ to higher-order Li₂S_n and the peak at 2.02 V corresponds to the additional reduction of these Li₂S_n to lower-order Li₂S and Li₂S₂[38, 39]. Simultaneously, there is only one clear oxidation peak at 2.45 V corresponding to the anodic scanning, which is related to oxidation process of Li₂S/Li₂S₂ to Li₂S_n[40]. After two cycles, the CV peak positions of the third and fourth cycles nearly overlap, indicating the superior electrochemical reversibility of C-MoS₂/rGO-6-S cathode.

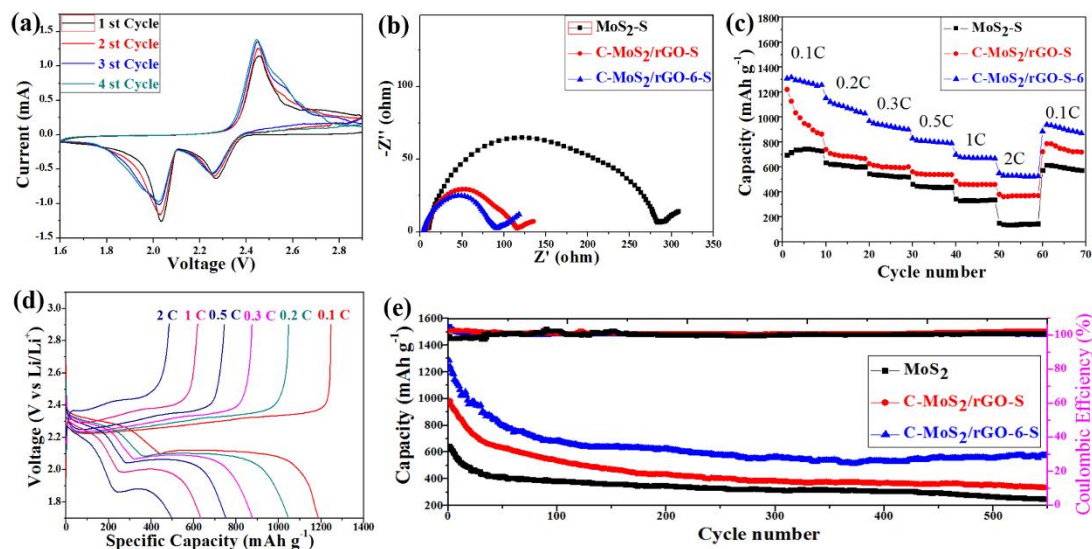


Fig. 6 (a) Typical CV curves of the C-MoS₂/rGO-6-S (b) Nyquist plots of MoS₂-S, C-MoS₂/rGO-S and C-MoS₂/rGO-6-S composites over a frequency range 100 kHz to 0.01 Hz. (c) Comparison of rate capabilities at different C-rates for MoS₂-S, C-MoS₂/rGO-S and C-MoS₂/rGO-6-S composites (d) Charge/discharge curves of C-MoS₂/rGO-6-S at varied C rates (e) Discharge capacities and coulombic efficiency for MoS₂-S, C-MoS₂/rGO-S and C-MoS₂/rGO-6-S composites at a rate of 0.2C.

To better understand the enhanced electrochemical performance of the C-MoS₂/rGO-6-S composite, the electrochemical impedance spectroscopy analysis of MoS₂-S, C-MoS₂/rGO-S, C-MoS₂/rGO-6-S electrodes are showed in Fig. 6b. Obviously, the C-MoS₂/rGO-S and C-MoS₂/rGO-6-S electrodes have the minor semicircles in the high-frequency range, suggesting the smaller charge transfer resistance compared with MoS₂-S. Since every cathode holds the same amount of sulfur, the distinct charge transfer resistance could be ascribed to the conductivity of the different host materials. Benefiting from the synergistic encapsulation of the polar MoS₂ nanosheet and conductive amorphous carbon and rGO, C-MoS₂/rGO-6-S shows

stronger chemical interaction with Li_2S_n and better ability to assist the charge transfer electrode than the $\text{MoS}_2\text{-S}$ and $\text{C-MoS}_2/\text{rGO-S}$ electrode.

Furthermore, the rate capabilities of the $\text{MoS}_2\text{-S}$, $\text{C-MoS}_2/\text{rGO-S}$, $\text{C-MoS}_2/\text{rGO-6-S}$ electrodes are respectively measured in the galvanostatic mode at several charge–discharge rates, and the corresponding capacities calculated are shown in Fig. 6c and Fig. S4b. The $\text{C-MoS}_2/\text{rGO-6-S}$ electrode indicates higher capacity than the $\text{MoS}_2\text{-S}$, $\text{C-MoS}_2/\text{rGO-S}$, $\text{C-MoS}_2/\text{rGO-4-S}$ and $\text{C-MoS}_2/\text{rGO-8-S}$ electrodes in the total charge–discharge process. A discharge capacity of 694, 1221, 1309, 1142, and 734 mA h g^{-1} is respectively achieved for the $\text{MoS}_2\text{-S}$, $\text{C-MoS}_2/\text{rGO-S}$, $\text{C-MoS}_2/\text{rGO-6-S}$, $\text{C-MoS}_2/\text{rGO-4-S}$, and $\text{C-MoS}_2/\text{rGO-8-S}$ electrodes after the first cycle at 0.1C. The $\text{C-MoS}_2/\text{rGO-6-S}$ electrode still shows a reversible capacity of 551 mA h g^{-1} even at the elevated discharge and charge rate (C-rate) of 2C, indicating better rate capability. The capacity of 939 mA h g^{-1} is retained for the $\text{C-MoS}_2/\text{rGO-6-S}$ electrode, approximately 72% capacity retention of the initial capacity after the C-rate was adjusted back to 0.1C. As contrast, the $\text{MoS}_2\text{-S}$ and $\text{C-MoS}_2/\text{rGO-S}$ electrodes indicate noticeably lower discharge capacities in the range from 0.1 to 2C. For the $\text{MoS}_2\text{-S}$, this is ascribed to its lower electronic conductivity, leading to inferior utilization to sulfur and polysulfides. Compared with $\text{C-MoS}_2/\text{rGO-S}$, the significant improvement of the capacity of $\text{C-MoS}_2/\text{rGO-6-S}$ electrodes can be attributed to the annealing treatment, which can not only reduce amorphous carbon and GO but also enhance synergistic effects and thus results in additional powerful polar–polar chemical interaction rather than only the weak physical adsorption for the polysulfides [8]. The galvanostatic discharge–charge

curves of C-MoS₂/rGO-6-S at several current densities are illustrated in Fig. 4d. The two standard discharge plateaus can still be visibly identified even at rate of 2C, indicating the effortless kinetics of the sulfur redox reaction.

Fig. 6e and Fig. S4c compare the cyclic performances of the MoS₂-S, C-MoS₂/rGO-S, C-MoS₂/rGO-6-S and C-MoS₂/rGO-4-S, C-MoS₂/rGO-8-S at 0.2 C, respectively. All sample showed rapid decay in the initial stage. Only the C-MoS₂/rGO-6-S composite exhibits the largest initial specific capacity due to the large number of mesoporous. The mesoporous can contain more electrolyte to form a good infiltration with the sulfur on the surface and mesoporous of composite, so that the sulfur can more fully discharge the reaction during the initial several cycles. However, since the discharge reaction causes a part of the polysulfide ions to dissolve and continuously enter the electrolyte, the sulfur is also continuously lost. Consequently, a rapid decay of the specific capacity occurs when the composite is loaded with less sulfur. After several cycles of charge and discharge, the dissolved polysulfide ions in the electrolyte will reach a dynamic equilibrium. The dissolution of polysulfide ions into the electrolyte will be gradually restrained during the subsequent charge and discharge reaction. Therefore, the less the specific capacity is suppressed. Furthermore, the charge and discharge cycle can maintain a relatively stable state.

It is worth noting that the initial discharge specific capacities of MoS₂, C-MoS₂/rGO, and C-MoS₂/rGO-6 composites are 643, 975, and 1285 mA h g⁻¹, respectively, and the specific capacities after 550 cycles are 249, 334, and 572 mA h g⁻¹, respectively. This shows that the combination of MoS₂, amorphous carbon and rGO

not only has an ultra-high specific surface area but also enhances conductivity. At the same time, the C-MoS₂/rGO-6 composite exhibits ultra-high stability and high specific capacity, which suggests the excellent catalytic performance of the defect rich MoS₂ for polysulfide ion.

Conclusion

The defect-rich porous C-MoS₂/rGO composites have been successfully fabricated via double modification by rGO and amorphous carbon layers. The catalytic capability of polysulfide conversion has been improved apparently. The subsequent annealing at 600 °C enhances the synergistic effect between MoS₂ and rGO and amorphous carbon and further improves the capability of polysulfide conversion. This work provides reference for fabrication and design of electrodes for Li-S battery and TMD electrodes for energy storage.

Acknowledgements

This work is financially supported by the NSAF Joint Foundation of China (Grant No. U1630126).

Appendix A. Supplementary data

Supplementary data associated with this article available.

References

- [1] T. Lei, W. Chen, J. Huang, C. Yan, H. Sun, C. Wang, W. Zhang, Y. Li, J. Xiong, Multi-Functional Layered WS₂ Nanosheets for Enhancing the Performance of Lithium-Sulfur Batteries, *Adv. Energy Mater.* 7 (2017) 1601843.

- [2] J. Pu, Z. Shen, J. Zheng, W. Wu, C. Zhu, Q. Zhou, H. Zhang, F. Pan, Multifunctional Co_3S_4 @sulfur nanotubes for enhanced lithium-sulfur battery performance, *Nano Energy* 37 (2017) 7-14.
- [3] H. Lin, L. Yang, X. Jiang, G. Li, T. Zhang, Q. Yao, G.W. Zheng, J.Y. Lee, Electrocatalysis of polysulfide conversion by sulfur-deficient MoS_2 nanoflakes for lithium-sulfur batteries, *Energy Environ. Sci.* 10 (2017) 1476-1486.
- [4] Q. Pang, X. Liang, C.Y. Kwok, L.F. Nazar, Advances in lithium-sulfur batteries based on multifunctional cathodes and electrolytes, *Nat. Energy* 1 (2016).
- [5] Y.X. Yin, S. Xin, Y.G. Guo, L.J. Wan, Lithium-sulfur batteries: electrochemistry, materials, and prospects, *Angew. Chem. Int. Edit.* 52 (2013) 13186-13200.
- [6] Highly Conductive and Lightweight Composite Film as Polysulfide Reservoir for High-Performance Lithium-Sulfur Batteries, *ChemElectroChem* (2016).
- [7] G. Hu, C. Xu, Z. Sun, S. Wang, H.M. Cheng, F. Li, W. Ren, 3D Graphene-Foam-Reduced-Graphene-Oxide Hybrid Nested Hierarchical Networks for High-Performance Li-S Batteries, *Adv. Mater.* 28 (2016) 1603-1609.
- [8] M. Fang, Z. Chen, Y. Liu, J. Quan, C. Yang, L. Zhu, Q. Xu, Q. Xu, Design and synthesis of novel sandwich-type $\text{C@TiO}_2\text{@C}$ hollow microspheres as efficient sulfur hosts for advanced lithium-sulfur batteries, *J. Mater. Chem. A* 6 (2018) 1630-1638.
- [9] J.Z. Wang, L. Lu, M. Choucair, J.A. Stride, X. Xu, H.K. Liu, Sulfur-graphene composite for rechargeable lithium batteries, *J. Power Sources* 196 (2011) 7030-7034.

- [10] J.-Q. Huang, Q. Zhang, H.-J. Peng, X.-Y. Liu, W.-Z. Qian, F. Wei, Ionic shield for polysulfides towards highly-stable lithium–sulfur batteries, *Energy Environ. Sci.* 7 (2014) 347-353.
- [11] L. Qie, A. Manthiram, A facile layer-by-layer approach for high-areal-capacity sulfur cathodes, *Adv. Mater.* 27 (2015) 1694-1700.
- [12] H. Yao, K. Yan, W. Li, G. Zheng, D. Kong, Z.W. Seh, V.K. Narasimhan, Z. Liang, Y. Cui, Improved lithium–sulfur batteries with a conductive coating on the separator to prevent the accumulation of inactive S-related species at the cathode–separator interface, *Energy Environ. Sci.* 7 (2014) 3381-3390.
- [13] Y.C. Jeong, J.H. Kim, S.H. Kwon, J.Y. Oh, J. Park, Y. Jung, S.G. Lee, S.J. Yang, C.R. Park, Rational design of exfoliated 1T MoS₂@CNT-based bifunctional separators for lithium sulfur batteries, *J. Mater. Chem. A* 5 (2017) 23909-23918.
- [14] P. Guo, D. Liu, Z. Liu, X. Shang, Q. Liu, D. He, Dual functional MoS₂/graphene interlayer as an efficient polysulfide barrier for advanced lithium-sulfur batteries, *Electrochim. Acta* 256 (2017) 28-36.
- [15] Z.A. Ghazi, X. He, A.M. Khattak, N.A. Khan, B. Liang, A. Iqbal, J. Wang, H. Sin, L. Li, Z. Tang, MoS₂/Celgard Separator as Efficient Polysulfide Barrier for Long-Life Lithium-Sulfur Batteries, *Adv. Mater.* 29 (2017).
- [16] F. Sun, H. Tang, B. Zhang, X. Li, C. Yin, Z. Yue, L. Zhou, Y. Li, J. Shi, PEO-Linked MoS₂–Graphene Nanocomposites with 2D Polar–Nonpolar Amphoteric Surfaces as Sulfur Hosts for High-Performance Li–S Batteries, *ACS Sustain. Chem. Eng.* 6 (2017) 974-982.

- [17] Z. Li, J. Zhang, B. Guan, D. Wang, L.M. Liu, X.W. Lou, A sulfur host based on titanium monoxide@carbon hollow spheres for advanced lithium-sulfur batteries, *Nat. Commun.* 7 (2016) 13065.
- [18] J.D. Benck, T.R. Hellstern, J. Kibsgaard, P. Chakthranont, T.F. Jaramillo, Catalyzing the Hydrogen Evolution Reaction (HER) with Molybdenum Sulfide Nanomaterials, *ACS Catal.* 4 (2014) 3957-3971.
- [19] X. Zhang, Z.C. Lai, C.L. Tan, H. Zhang, Solution-Processed Two-Dimensional MoS₂ Nanosheets: Preparation, Hybridization, and Applications, *Angew. Chem. Int. Edit.* 55 (2016) 8816-8838.
- [20] Z. Zhang, W. Li, M.F. Yuen, T.-W. Ng, Y. Tang, C.-S. Lee, X. Chen, W. Zhang, Hierarchical composite structure of few-layers MoS₂ nanosheets supported by vertical graphene on carbon cloth for high-performance hydrogen evolution reaction, *Nano Energy* 18 (2015) 196-204.
- [21] W. Lai, Z. Chen, J. Zhu, L. Yang, J. Zheng, X. Yi, W. Fang, A NiMoS flower-like structure with self-assembled nanosheets as high-performance hydrodesulfurization catalysts, *Nanoscale* 8 (2016) 3823-3833.
- [22] A. Bruix, H.G. Fuchtbauer, A.K. Tuxen, A.S. Walton, M. Andersen, S. Porsgaard, F. Besenbacher, B. Hammer, J.V. Lauritsen, In Situ Detection of Active Edge Sites in Single-Layer MoS₂ Catalysts, *ACS Nano* 9 (2015) 9322-9330.
- [23] Y.X. Guo, X.Y. Zhang, X.P. Zhang, T.Y. You, Defect- and S-rich ultrathin MoS₂ nanosheet embedded N-doped carbon nanofibers for efficient hydrogen evolution, *J. Mater. Chem. A* 3 (2015) 15927-15934.

- [24] B. Chen, H.H. Lu, N.Q. Zhao, C.S. Shi, E.Z. Liu, C.N. He, L.Y. Ma, Facile synthesis and electrochemical properties of continuous porous spheres assembled from defect-rich, interlayer-expanded, and few-layered MoS₂/C nanosheets for reversible lithium storage, *J. Power Sources* 387 (2018) 16-23.
- [25] J. Xie, H. Zhang, S. Li, R. Wang, X. Sun, M. Zhou, J. Zhou, X.W. Lou, Y. Xie, Defect-rich MoS₂ ultrathin nanosheets with additional active edge sites for enhanced electrocatalytic hydrogen evolution, *Adv. Mater.* 25 (2013) 5807-5813.
- [26] Y. Zhang, S. Yu, H. Wang, Z. Zhu, Q. Liu, E. Xu, D. Li, G. Tong, Y. Jiang, A novel carbon-decorated hollow flower-like MoS₂ nanostructure wrapped with RGO for enhanced sodium-ion storage, *Chem. Eng. J.* 343 (2018) 180-188.
- [27] K.K. Liu, W. Zhang, Y.H. Lee, Y.C. Lin, M.T. Chang, C.Y. Su, C.S. Chang, H. Li, Y. Shi, H. Zhang, C.S. Lai, L.J. Li, Growth of large-area and highly crystalline MoS₂ thin layers on insulating substrates, *Nano Lett.* 12 (2012) 1538-1544.
- [28] C. Wang, W. Wan, Y. Huang, J. Chen, H.H. Zhou, X.X. Zhang, Hierarchical MoS₂ nanosheet/active carbon fiber cloth as a binder-free and free-standing anode for lithium-ion batteries, *Nanoscale* 6 (2014) 5351-5358.
- [29] D. Xie, W. Tang, Y. Wang, X. Xia, Y. Zhong, D. Zhou, D. Wang, X. Wang, J. Tu, Facile fabrication of integrated three-dimensional C-MoSe₂/reduced graphene oxide composite with enhanced performance for sodium storage, *Nano Res.* 9 (2016) 1618-1629.

- [30] L. Yang, W. Zhou, J. Lu, D. Hou, Y. Ke, G. Li, Z. Tang, X. Kang, S. Chen, Hierarchical spheres constructed by defect-rich MoS₂/carbon nanosheets for efficient electrocatalytic hydrogen evolution, *Nano Energy* 22 (2016) 490-498.
- [31] X. Dai, K. Du, Z. Li, H. Sun, Y. Yang, W. Zhang, X. Zhang, Enhanced hydrogen evolution reaction on few-layer MoS₂ nanosheets-coated functionalized carbon nanotubes, *Int. J. Hydrogen Energ* 40 (2015) 8877-8888.
- [32] G. Yue, X. Ma, Q. Jiang, F. Tan, J. Wu, C. Chen, F. Li, Q. Li, PEDOT:PSS and glucose assisted preparation of molybdenum disulfide/single-wall carbon nanotubes counter electrode and served in dye-sensitized solar cells, *Electrochim. Acta* 142 (2014) 68-75.
- [33] Y. Wang, Z. Ma, Y. Chen, M. Zou, M. Yousaf, Y. Yang, L. Yang, A. Cao, R.P. Han, Controlled Synthesis of Core-Shell Carbon@MoS₂ Nanotube Sponges as High-Performance Battery Electrodes, *Adv. Mater.* 28 (2016) 10175-10181.
- [34] J. Wang, J. Liu, D. Chao, J. Yan, J. Lin, Z.X. Shen, Self-assembly of honeycomb-like MoS₂ nanoarchitectures anchored into graphene foam for enhanced lithium-ion storage, *Adv. Mater.* 26 (2014) 7162-7169.
- [35] Y.X. Guo, L.F. Gan, C.S. Shang, E.K. Wang, J. Wang, A Cake-Style CoS₂@MoS₂/RGO Hybrid Catalyst for Efficient Hydrogen Evolution, *Adv. Funct. Mater.* 27 (2017) 1602699.
- [36] J. Zhang, T. Wang, D. Pohl, B. Rellinghaus, R. Dong, S. Liu, X. Zhuang, X. Feng, Interface Engineering of MoS₂/Ni₃S₂ Heterostructures for Highly Enhanced

Electrochemical Overall-Water-Splitting Activity, *Angew. Chem. Int. Edit.* 55 (2016) 6701-6706.

[37] D. Xie, D.H. Wang, W.J. Tang, X.H. Xia, Y.J. Zhang, X.L. Wang, C.D. Gu, J.P. Tu, Binder-free network-enabled MoS₂-PPY-rGO ternary electrode for high capacity and excellent stability of lithium storage, *J. Power Sources* 307 (2016) 510-518.

[38] Y. You, Y.W. Ye, M.L. Wei, W.J. Sun, Q. Tang, J. Zhang, X. Chen, H.Q. Li, J. Xu, Three-dimensional MoS₂/rGO foams as efficient sulfur hosts for high-performance lithium-sulfur batteries, *Chem. Eng. J.* 355 (2019) 671-678.

[39] X. Li, K. Zhao, L. Zhang, Z. Ding, K. Hu, MoS₂-decorated coaxial nanocable carbon aerogel composites as cathode materials for high performance lithium-sulfur batteries, *J. Alloy. Compd.* 692 (2017) 40-48.

[40] L. Tan, X. Li, Z. Wang, H. Guo, J. Wang, Lightweight Reduced Graphene Oxide@MoS₂ Interlayer as Polysulfide Barrier for High-Performance Lithium-Sulfur Batteries, *ACS Appl. Mater. Inter.* (2018).